Chemical Engineering Journal 519 (2025) 165230

Contents lists available at ScienceDirect

Chemical Engineering Journal

journal homepage: www.elsevier.com/locate/cej

Integration of Ti_3C_2/TiO_2 and spinel high-entropy oxide: A novel strategy for enhancing lithium-ion battery performance

Yingying Lu [a], Yi Zhang [a], Hailong Yan [a,*], Paul K. Chu [b], Jinbing Cheng [a,*], Yongsong Luo [a,*]

[a] Henan International Joint Laboratory of MXene Materials Microstructure, Nanyang Normal University, Nanyang 473061, China
[b] Department of Physics, Department of Materials Science & Engineering, and Department of Biomedical Engineering, City University of Hong Kong, Tat Chee Avenue, Kowloon, Hong Kong, China

ARTICLE INFO

Keywords:
Lithium-ion battery
High-entropy oxide
Ti_3C_2/TiO_2
Electrospinning

ABSTRACT

High entropy oxides (HEOs) exhibit stable thermochemical properties, superior mechanical characteristics, and favorable electrical and optical properties that are particularly significant for application in lithium-ion batteries (LIBs). The chemical composition of HEOs is tunable, enabling an exploration of a wide array of elemental combinations for the development of novel electrode materials. In this study, HEO@Ti_3C_2/TiO_2 nanofibers (HEO@Ti_3C_2/TiO_2 NFs) based on a spinel-structured HEO ($(MnCoNiCuZnFe)_3O_4$) were designed and synthesized *via* an electrostatic spinning process. The resultant HEO and Ti_3C_2/TiO_2 three-dimensional conductive network exhibited a significant enhancement of the charge transfer efficiency, which plays an important role in the LIB cycling process. *In situ* X-ray diffraction (XRD) analysis has confirmed that the spinel lattice was stable during cycling, which is attributed to an interfacial synergistic effect that facilitates reversible lithium storage.

1. Introduction

Global warming and the overconsumption of fossil fuels have significantly increased the level of carbon dioxide in the atmosphere. The consequent environmental impact and energy issues represent a serious challenge, which has driven the demand for sustainable energy solutions. In this context, the development of efficient energy storage technologies (*e.g.*, lithium-ion batteries (LIBs), supercapacitors, and electrocatalytic systems) is crucial to achieving carbon neutrality [1–3]. Rechargeable LIBs have an important role to play in the development of clean energy networks [4,5]. In order to address the current capacity bottleneck, researchers have focused on silicon-based alloy materials and transition metal oxides (TMOs) [6–11]. Although these materials offer significant theoretical advantages, the marked volume expansion (~300% for Si) during lithiation leads to solid electrolyte interface (SEI) membrane rupture and electrode pulverization, which severely impairs cycling stability. Nanostructured designs are effective in relieving mechanical stress by building an internal buffer space that enhances interfacial stability. Electrostatic spinning technology has emerged as the preferred method for the preparation of high-performance nanofiber electrodes, enabling a precise tuning of morphology (fiber diameter = 10 nm-2 μm), with low environmental impact, and feasible scale-up [12–15].

High entropy oxides (HEOs), as an emerging multicomponent material system, exhibit an entropy stabilization effect ($\Delta Sconfig \geq 1.5R$) involving more than five metal elements. The associated single-phase solid solution structure endows the material with high mechanical strength and slow kinetic decay, where the multiple redox active sites contribute to an ultra-high theoretical capacity [16–19]. Shin et al. prepared an HEO using a one-step combustion synthesis strategy with a precisely tuned ratio of fuel to oxidant. Application of the resultant HEO as a LIB anode generated a specific capacity of 791 mAh g^{-1} at a high current density (3 A g^{-1}) [20]. Triolo et al. developed $(Mn_{0.2}Fe_{0.2}Co_{0.2}Ni_{0.2}Zn_{0.2})_3O_4$ nanofibers that retained a capacity of 155 mAh g^{-1} after 550 cycles at 0.5 A g^{-1} [21]. In addition, Wang et al. designed a hollow porous $(NiCoCuFeMg)_3O_4$ that delivered 100% capacity retention at 2 A g^{-1} for 300 cycles [22]. However, the intrinsic low conductivity and limited active site utilization serve to severely limit HEO multiplicity performance and long cycle life [23–27].

The charge transfer kinetics can be modified by combining HEOs with highly conductive substrates in composite materials. Two-dimensional transition metal carbides (MXene) show significant advantages in this respect due to their unique layered structure, ultra-high conductivity and functionalized surfaces [28–30]. Tian et al. have

* Corresponding authors.
E-mail addresses: yanhailong2005@126.com (H. Yan), chengjinbing1988@163.com (J. Cheng), eysluo@163.com (Y. Luo).

https://doi.org/10.1016/j.cej.2025.165230
Received 23 March 2025; Received in revised form 20 June 2025; Accepted 22 June 2025
Available online 23 June 2025

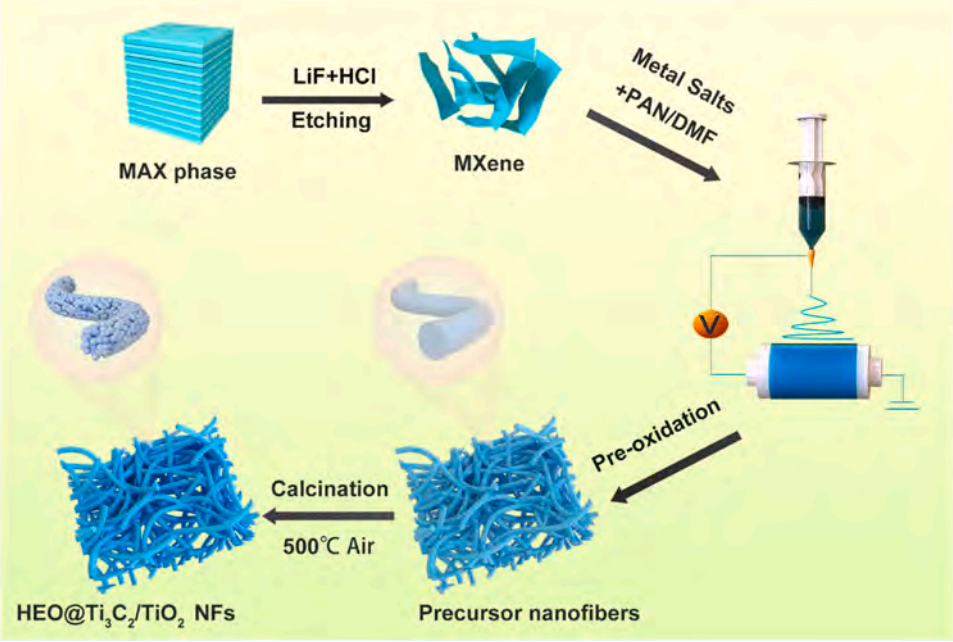

Fig. 1. Schematic representation of the multistep preparation of HEO@Ti_3C_2/TiO_2 nanocomposites.

proposed a novel synergistic strategy involving an *in situ* anchoring of barium titanate ferroelectric nanoparticles on few-layer Ti_3C_2 nanosheets by hydrothermal treatment, where the resulting composites exhibited superior cycling and multiplicative properties [31]. Moreover, Yang and co-workers have successfully anchored tin-based metal-organic frameworks (Sn-MOFs) in a uniform arrangement on the surface

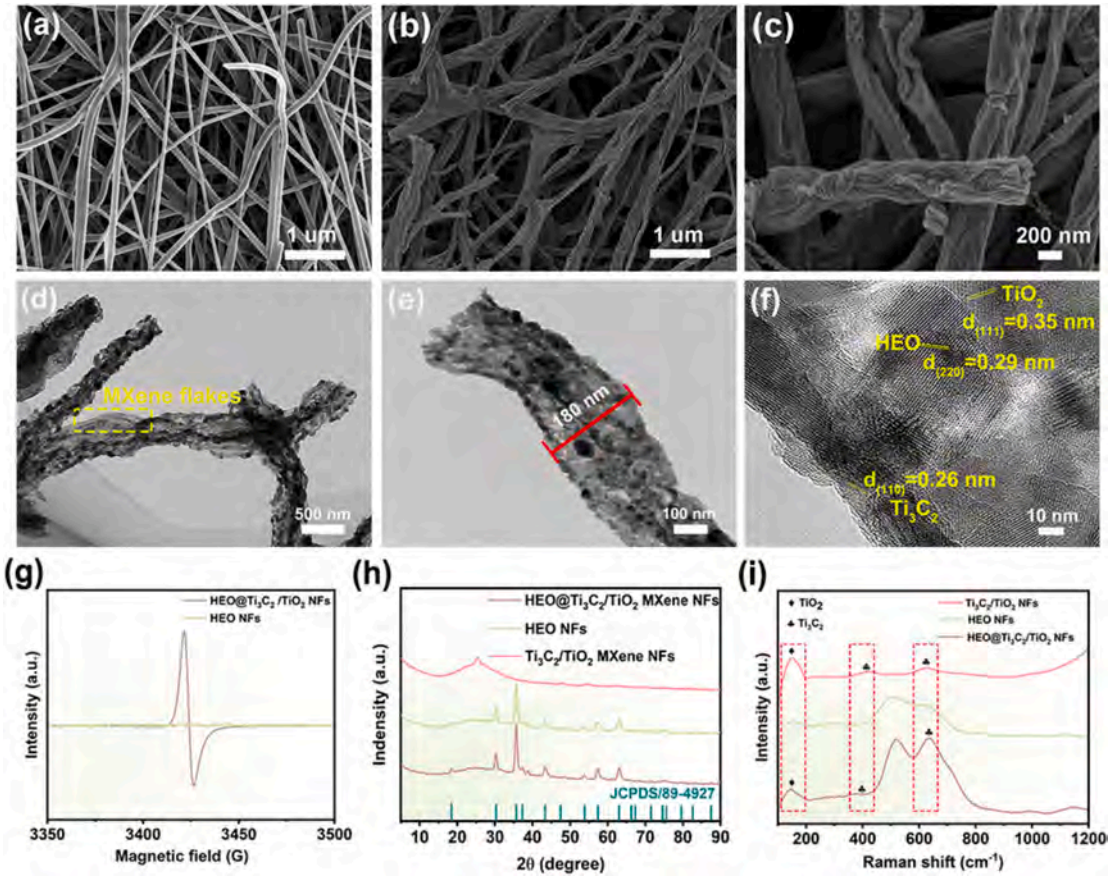

Fig. 2. (a-c) SEM images of HEO@Ti_3C_2/TiO_2 NFs; (d-e) TEM images of HEO@Ti_3C_2/TiO_2 NFs; (f) HR-TEM image of HEO@Ti_3C_2/TiO_2 NFs; (g) EPR spectra of HEO@Ti_3C_2/TiO_2 NFs and HEO NFs; (h) XRD patterns of HEO@Ti_3C_2/TiO_2 NFs, HEO NFs, and Ti_3C_2/TiO_2 NFs; (i) Raman scattering spectra of HEO@Ti_3C_2/TiO_2 NFs, HEO NFs, and Ti_3C_2/TiO_2 NFs.

of MXene nanosheets [32]. A low-temperature *in-situ* growth synthesis was utilized to construct a stable structure for ultrafast Li-ion storage. Based on the literature, a composite of HEO with Ti_3C_2/TiO_2 should enhance the electrochemical performance of HEOs.

The goal of achieving a strong coupling of HEO with MXene through controlled interfacial engineering that can promote and synergistically optimize the conductive network while ensuring structural stability represents a major research challenge. Currently, studies dealing with the combination of highly conductive substrates with HEOs are limited. There is a clear demand for in-depth theoretical analysis, comprehensive experimental measurements, and the development of innovative research methods.

In this study, a high entropy design strategy has been employed, where six major elements (Mn, Co, Ni, Cu, Zn and Fe) were selected to maximize the conformational entropy. Inductively coupled plasma optical emission spectroscopy (ICP-OES) (Table S1) and configuration entropy (Eq. (S1)) analyses have confirmed a maximum entropy value of $\Delta Sconfig = 1.79R$, which contributes to the successful synthesis of spinel structure. As illustrated in Fig. 1, the proposed synthesis protocol integrates an electrostatic spinning process, establishing a novel pathway for fabricating HEO/MXene composites. The preparation of ultrathin Ti_3C_2 MXene flakes has involved a selective etching and delamination of the Ti_3AlC_2 MAX phase precursor. In a *N*, *N*-dimethylformamide (DMF) solution, the hydroxyl (-OH) and fluorine (—F) functional groups on the MXene surface formed stable complexes with metal salts *via* electrostatic interactions. Hydrogen bonding between MXene and polyacrylonitrile (PAN) polymer chains ensured molecular-level homogenization of the metal salts and MXene in the electrospinning solution. Under an applied electric field, these components synergistically self-assembled into continuous nanofiber precursors. In a pre-oxidation at 250 °C, PAN underwent cyclization and dehydrogenation to form a trapezoidal carbon skeleton, ensuring structural integrity in subsequent high-temperature processing. Calcination at 500 °C promoted the crystallization of metal salts into HEO nanoparticles with concomitant PAN decomposition. Partial surface oxidation of MXene generated TiO_2, facilitating an *in situ* construction of heterointerfaces where HEO nanoparticles were firmly anchored to MXene *via* robust chemical bonds and were partially embedded in the nanofibers. This configuration establishes a strong interfacial coupling that effectively suppresses nanoparticle agglomeration while enhancing structural stability. The ultrathin Ti_3C_2/TiO_2 layers were intricately interwoven within the nanofiber matrix, forming continuous conductive pathways that, in conjunction with the HEO nanoparticles, markedly reduced charge transfer resistance. The synergistic anchoring and embedding of HEO nanoparticles result in compositional homogeneity, strong interfacial bonding, and overall structural integrity. The fabricated HEO@Ti_3C_2/TiO_2 NFs electrode delivered superior electrochemical performance, retaining a specific capacity of 305.9 mAh g^{-1} after 1000 cycles at a current density of 2 A g^{-1}.

2. Results and discussion

The field-emission scanning electron microscopy (FE-SEM) image of Ti_3AlC_2, shown in Fig. S1a, reveals a flake-like morphology. The layered structure of Ti_3C_2 flakes following etching Ti_3AlC_2 with lithium fluoride and hydrofluoric acid is shown in Fig. S1b. The formation of TiO_2 on the Ti_3C_2 flakes after calcination at 500 °C in air is demonstrated in Fig. S1c, where MXene retains a nanosheet structure. The influence of the MXene lamellar structure on the nanofibers was assessed in a systematic investigation directed at optimizing MXene addition to achieve a homogeneous nanofiber morphology. As shown in Fig. S2, the addition of 1 mL Ti_3C_2 resulted in appreciable nanofiber morphological inhomogeneity. Increasing the addition to 3 mL led to extensive fiber aggregation. In repeated synthesis and analyses, a 2 mL Ti_3C_2 addition was determined as optimal, producing HEO@Ti_3C_2/TiO_2 NFs with the targeted morphological characteristics.

Detailed structural characterization of the HEO@Ti_3C_2/TiO_2 NFs is presented in Fig. 2. Scanning electron microscopy (SEM) was employed to determine the morphology of the as-synthesized precursor fibers and the nanofibers following calcination at 500 °C. The HEO@Ti_3C_2/TiO_2 NFs precursor exhibits a uniformly smooth surface (Fig. 2a). The morphology of the HEO@Ti_3C_2/TiO_2 NFs after calcination at 500 °C is shown in Fig. 2b-c. Metal salt crystallization to form HEO accompanied by PAN decomposition resulted in a weight loss of 86.14% (Fig. S3). The partial oxidation of the MXene surface led to an *in-situ* formation of TiO_2 and the generation of a heterojunction interface. In this process, HEO nanoparticles were uniformly anchored on the surface of Ti_3C_2/TiO_2 and partially embedded in the fibers, forming a strong interfacial coupling that effectively inhibited aggregation and enhanced structural stability.

Transmission electron microscopy (TEM) was utilized to further characterize the nanostructure and chemical composition of the HEO@Ti_3C_2/TiO_2 NFs composite. The TEM image presented in Fig. 2d shows the distribution of HEO nanoparticles and Ti_3C_2/TiO_2 nanosheets. The TEM image given in Fig. 2e reveals the presence of nanofibers with an average diameter of approximately 180 nm, which are rich in HEO nanocrystals. The selected-area electron diffraction (SAED) pattern (Fig. S4) presents diffraction rings that correspond solely to the spinel structure of HEO.

The high-resolution TEM (HRTEM) image in Fig. 2f exhibits clear lattice fringes with spacings of approximately 0.29, 0.35, and 0.26 nm that can be attributed to the (220) plane of HEO, the (111) plane of TiO_2, and the (110) plane of Ti_3C_2, respectively. The uniform distribution of metals was confirmed by the corresponding energy-dispersive spectroscopy (EDS) mappings (Fig. S5). Collectively, these characterization measurements have established the effective integration of HEO and Ti_3C_2/TiO_2 nanosheets within the nanofibers. In addition, a detailed structural characterization of pure HEO NFs and Ti_3C_2/TiO_2 NFs was conducted, as shown in Figs. S6 and S7. The pure HEO NFs exhibited fragmented fiber structures and typical spinel lattices. The TEM analysis has revealed that the HEO NFs exhibited an average diameter of approximately 130 nm with evidence of abundant HEO nanoparticles (Fig. S6d). The HRTEM image (Fig. S6e), SAED pattern (Fig. S6f), and EDS mappings (Fig. S6g) confirmed an HEO NFs spinel structure with the homogeneous distribution of multiple major elements. The Ti_3C_2/TiO_2 NFs are characterized by a curved fiber morphology (Fig. S7a), with an average diameter of approximately 250 nm as determined by TEM (Fig. S7b). The HRTEM image (Fig. S7c) showed lattice spacings corresponding to the (111) plane of TiO_2 and the (110) plane of Ti_3C_2. The corresponding SAED pattern (Fig. S7d) was indexed to the diffraction rings of Ti_3C_2 and TiO_2. Moreover, EDS mappings (Fig. S7e) confirmed the uniform distribution of multiple major elements associated with Ti_3C_2/TiO_2 NFs.

When compared with the pure HEO NFs, the HEO@Ti_3C_2/TiO_2 NFs exhibited larger particle sizes and curved morphologies, confirming the successful combination of HEO and Ti_3C_2/TiO_2 nanosheets. Analysis of the N_2 adsorption-desorption isotherms (Fig. S8a) has established a specific surface area of 36.88 m^2 g^{-1} for HEO@Ti_3C_2/TiO_2 NFs, significantly higher than that (25.71 m^2 g^{-1}, Fig. S8b) recorded for pure HEO NFs. The higher specific surface area of HEO@Ti_3C_2/TiO_2 NFs serves to enhance the exposure of active sites with improved interfacial reaction kinetics. Electron paramagnetic resonance (EPR) spectroscopy was employed to evaluate oxygen vacancy concentrations. The characteristic signal at $g = 2.003$ corresponds to unpaired electrons trapped by oxygen vacancies, where the intensity is positively correlated with oxygen vacancy concentration [23]. As shown in Fig. 2g, the EPR signal intensity of HEO@Ti_3C_2/TiO_2 NFs was significantly higher than that of HEO NFs, indicating that the introduction of MXene induced the formation of oxygen vacancies, promoting interfacial charge transfer with enhanced charge transfer kinetics.

X-ray diffraction (XRD) measurements were conducted on the Ti_3AlC_2 MAX phase and the etched Ti_3C_2 MXene, as illustrated in Fig. S9a. The XRD pattern of Ti_3C_2 MXene exhibits a prominent

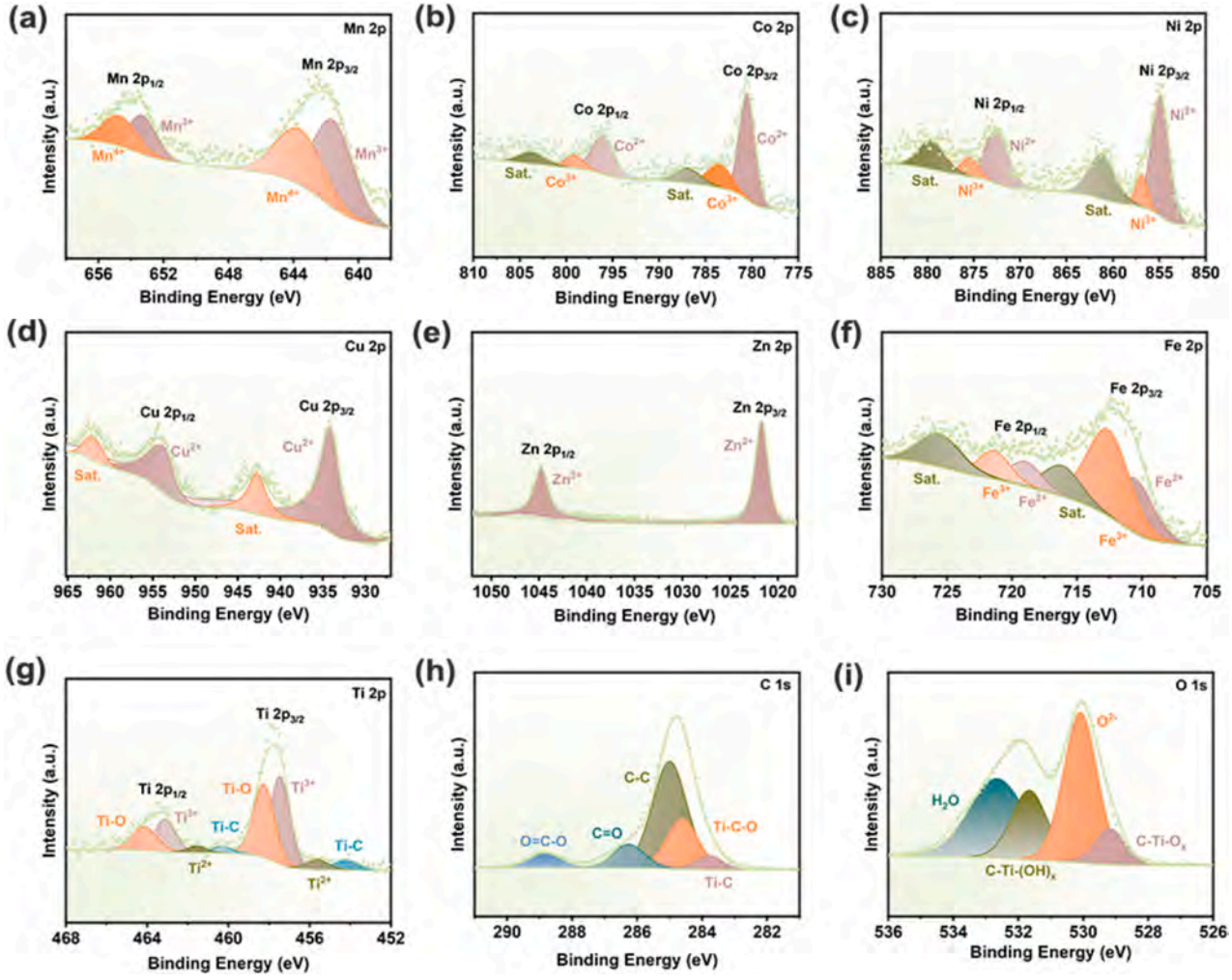

Fig. 3. XPS (a) Mn 2*p*, (b) Co 2*p*, (c) Ni 2*p*, (d) Cu 2*p*, (e) Zn 2*p*, (f) Fe 2*p*, (g) Ti 2*p*, (h) C 1*s*, and (i) O 1*s* spectra of HEO@Ti_3C_2/TiO_2 NFs.

characteristic peak at $2\theta = 6.8°$ corresponding to the (002) crystal plane. This peak originates from the layered structure stabilized by weak interlayer van der Waals forces, confirming the successful synthesis of Ti_3C_2 MXene. Following calcination in air, the appearance of a peak at $2\theta = 25.2°$ is associated with the (101) crystal plane of TiO_2. Concurrently, the intensity of the peak due to the (002) decreased significantly. These results suggest that during calcination, the surface oxidation of Ti_3C_2 leads to the formation of a TiO_2 layer, where the original lamellar structure is maintained. This observation provides valuable insight into the structural evolution of Ti_3C_2 MXene during thermal treatment [33].

The XRD patterns of HEO@Ti_3C_2/TiO_2 NFs, HEO NFs, and Ti_3C_2/TiO_2 NFs are presented in Fig. 2h. All three samples exhibit the presence of minor carbon residues. The XRD patterns of HEO and HEO@Ti_3C_2/TiO_2 NFs are consistent with a $NiFe_2O_4$ (JCPDS 89-4927) spinel structure. The six constituent (Mn, Co, Ni, Cu, Zn and Fe) ions occupy the spinel lattice (Fd-3m) to form a stable structure. The diffraction peaks at 18.41°, 30.28°, 35.69°, 37.35°, 43.34°, 53.84°, 57.42°, and 63.08° can be indexed to the (111), (220), (311), (222), (400), (422), (511), and (440) planes of the spinel. In the XRD pattern of Ti_3C_2/TiO_2 NFs, only the characteristic peak for TiO_2 at $2\theta = 25.2°$ is detected, and the signal due to the (002) crystal plane of Ti_3C_2 is not observed. As the MXene content is relatively low, following oxidation during calcination, the peak intensity may fall below the detection limit. In addition, coverage of the MXene surface by residual carbon and HEO nanoparticles may interfere with XRD detection of the weak signal associated with the (002) crystal plane. The EDS measurement of Ti_3C_2/TiO_2 NFs (Fig. S9b) further supports the above analysis in terms of elemental distribution.

In the Raman scattering spectrum (Fig. 2i), the peaks at 415 cm^{-1} and 625 cm^{-1} correspond to the vibrational modes of Ti_3C_2, whereas the peak at 150 cm^{-1} is attributed to TiO_2 [26,34–36]. In the case of HEO NFs, the wavenumbers in the 400–700 cm^{-1} range converge in a broad peak associated with the lattice asymmetry and cation disorder of the high-entropy spinel [37–40]. The Raman spectrum of HEO@Ti_3C_2/TiO_2 NFs exhibits the vibrational modes of MXene and the HEO phase, confirming the successful fabrication of the composite.

The entries in Fig. S10 reveal the presence of nine elements in the composite. The Mn 2*p* XPS spectrum (Fig. 3a) exhibits peaks at 641.97 and 653.24 eV corresponding to Mn^{3+} $2p_{3/2}$ and Mn^{3+} $2p_{1/2}$, whereas the peaks at 644.65 and 654.82 eV are associated with Mn^{4+} $2p_{3/2}$ and Mn^{4+} $2p_{1/2}$, respectively [41,42]. In the Co 2*p* spectrum (Fig. 3b), peaks due to Co^{2+} $2p_{3/2}$ (780.52 eV), Co^{2+} $2p_{1/2}$ (796.12 eV), Co^{3+} $2p_{3/2}$ (783.48 eV), and Co^{3+} $2p_{1/2}$ (799.28 eV) are observed in addition to the corresponding satellite peaks at 786.94 and 803.4 eV [43]. The Ni 2*p* spectrum (Fig. 3c) exhibits peaks attributed to Ni^{2+} $2p_{3/2}$ (854.87 eV), Ni^{2+} $2p_{1/2}$ (872.50 eV), Ni^{3+} $2p_{3/2}$ (856.90 eV), and Ni^{3+} $2p_{1/2}$ (875.32 eV) in addition to satellite peaks at 861.28 and 879.56 eV [43,44]. The Cu 2*p* spectrum (Fig. 3d) shows peaks for Cu^{2+} $2p_{3/2}$ (932.82 eV) and Cu^{2+} $2p_{1/2}$ (952.64 eV) with satellite peaks at 942.76 and 962.28 eV [45]. In the Zn 2*p* spectrum (Fig. 3e), the peaks at 1021.48 and 1044.62 eV correspond to Zn^{2+} $2p_{3/2}$ and Zn^{2+} $2p_{1/2}$, respectively. The Fe 2*p* spectrum (Fig. 3f) shows peaks at 710.52 and 718.95 eV for Fe^{2+} $2p_{3/2}$ and Fe^{2+} $2p_{1/2}$, peaks at 712.62 and 721.35 eV for Fe^{3+} $2p_{3/2}$ and Fe^{3+}

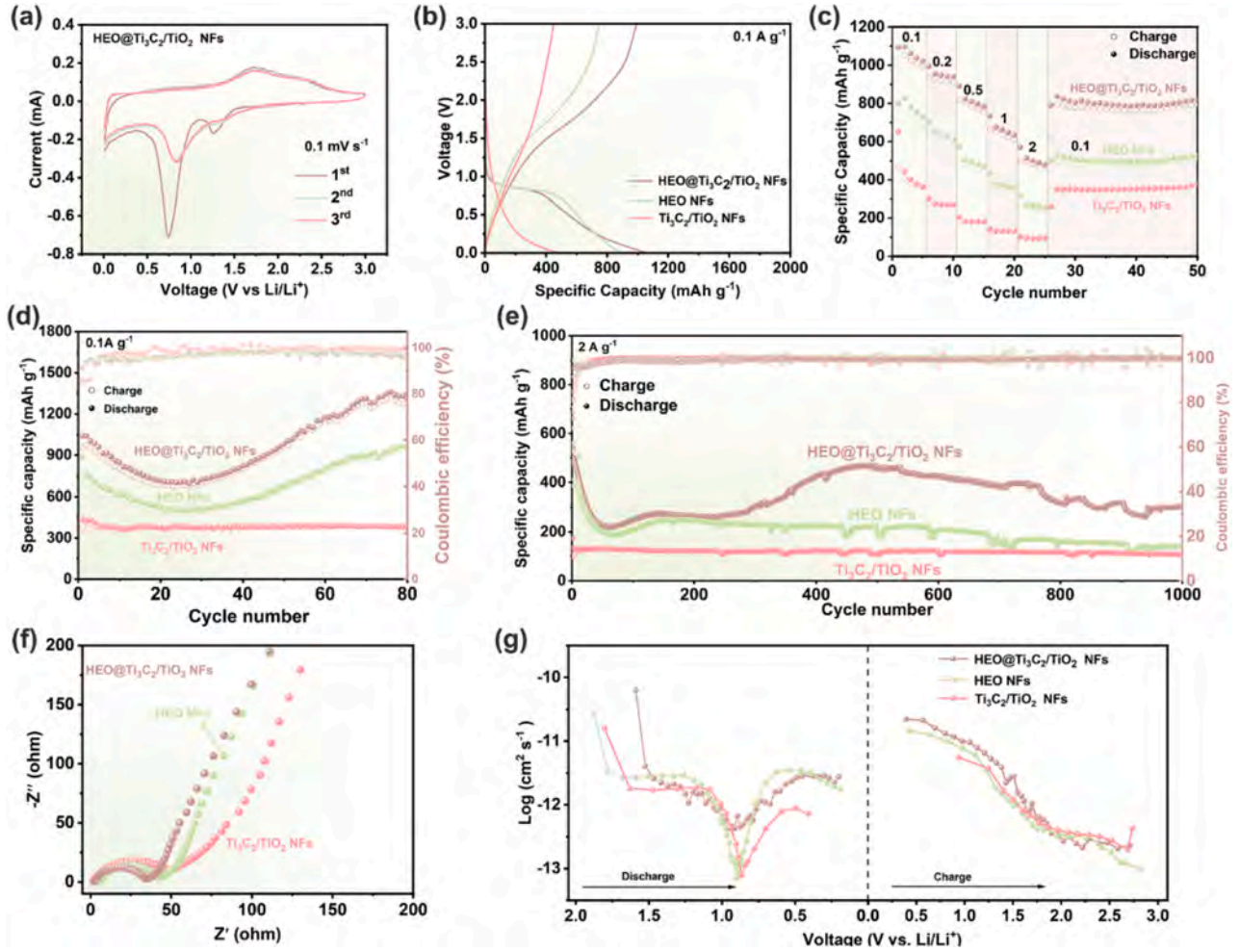

Fig. 4. (a) CVs of HEO@Ti_3C_2/TiO_2 NFs electrodes at 0.1 mV s^{-1}; (b) comparison of HEO@Ti_3C_2/TiO_2 NFs, HEO NFs, and Ti_3C_2/TiO_2 NFs at 0.1 A g^{-1} with respect to the first constant-current charging/discharging curves; (c) rate performance of HEO@Ti_3C_2/TiO_2 NFs, HEO/NFs, and Ti_3C_2/TiO_2 NFs; cycling performance of HEO@Ti_3C_2/TiO_2 NFs, HEO NFs, and Ti_3C_2/TiO_2 NFs at current densities of (d) 0.1 A g^{-1} and (e) 2 A g^{-1}; (f) EIS spectra and (g) GITT curves of HEO@Ti_3C_2/TiO_2 NFs, HEO NFs and Ti_3C_2/TiO_2 NFs.

$2p_{1/2}$, respectively, with satellite peaks at 716.15 and 726.62 eV [46]. The Ti 2*p* spectrum (Fig. 3g) shows four sets of peaks attributable to Ti—C (454.25 and 460.34 eV), Ti^{2+} (455.62 and 461.64 eV), Ti^{3+} (457.44 and 463.06 eV), and Ti—O (458.32 and 464.23 eV) that correspond to $2p_{3/2}$ and $2p_{1/2}$ [47,48]. In the case of the C1*s* spectrum (Fig. 3h), the peaks at 283.62, 284.41, 284.84, 285.82, and 288.32 eV may be ascribed to C—Ti, Ti = C=O, C—C, C=O, and O=C-O, respectively, for Ti_3C_2/TiO_2 [49]. The O 1 *s* XPS spectrum (Fig. 3i) shows peaks at 529.21 and 531.44 eV associated with C-Ti-Ox and C-Ti-$(OH)_x$ in $Ti_3C_2T_x$ MXene. The peak at 530.02 eV is related to metal-oxygen bonds, and the signal at 532.41 eV is attributed to hydroxyl or surface-adsorbed oxygen [47,50]. The XPS analysis confirms the successful synthesis of the HEO/Ti_3C_2/TiO_2 composite materials by electrospinning.

Application of the composite materials as anode materials in LIBs has been investigated. The three initial cyclic voltammetry (C*V*) curves of HEO@Ti_3C_2/TiO_2 NFs in the 0.01–3 V range and a scanning rate of 0.1 mV s^{-1} are shown in Fig. 4a. In the first cathodic scan, the peaks at 0.74 and 1.25 *V* correspond to the reduction of metal ions, formation of lithium oxide (Li_2O), establishment of the solid electrolyte interphase (SEI) layer, and irreversible changes to the crystal structure [46]. The observed response is consistent with an initial capacity drop during cycling. The oxidation peak at 1.78 *V* corresponds to the oxidation of active elements in high-entropy materials, where the broad peak indicates that oxidation may be a continuous process. In subsequent cycles, the reduction peaks are shifted to higher voltages. The cathodic (0.84/1.30 V) and anodic (1.78 V) peaks demonstrate good overlap, indicating enhanced structural stability and electrochemical reversibility.

The galvanostatic charge/discharge (GCD) curves of HEO@Ti_3C_2/TiO_2 NFs, HEO NFs, and Ti_3C_2/TiO_2 NFs at a current density of 0.1 A g^{-1} are shown in Fig. 4b. The HEO system exhibits a distinct voltage plateau at 0.8 V during the discharge process, which is related to the reduction of the metal elements in the HEO system and the formation of the SEI layer. This response is consistent with the results of the cyclic voltammetry measurements. It should be noted that the charge/discharge plateau for HEO@Ti_3C_2/TiO_2 NFs was shorter, which can be attributed to the synergistic effect involving MXene and HEO. The latter serves to optimize the overall electrical conductivity, reducing polarization, and increasing the rate of lithium-ion insertion/extraction. The rate performance of the three samples measured at current densities ranging from 0.1 to 2 A g^{-1} is presented in Fig. 4c. The capacities for all the samples decrease with increasing current density, due to limited diffusion-driven reactions at higher discharge currents. Each sample exhibited good rate stability. The HEO@Ti_3C_2/TiO_2 NFs delivered higher reversible specific capacities than HEO NFs and Ti_3C_2/TiO_2 NFs at current densities of 0.1, 0.2, 0.5, 1.0, and 2.0 A g^{-1}. When the current density returned to 0.1 A g^{-1}, the capacity reached 796 mAh g^{-1}.

The long-term cycling performance of HEO@Ti_3C_2/TiO_2 NFs, pure HEO NFs, and Ti_3C_2/TiO_2 NFs at a current density of 0.1 A g^{-1} is illustrated in Fig. 4d. The data reveal that the nanofiber electrodes based

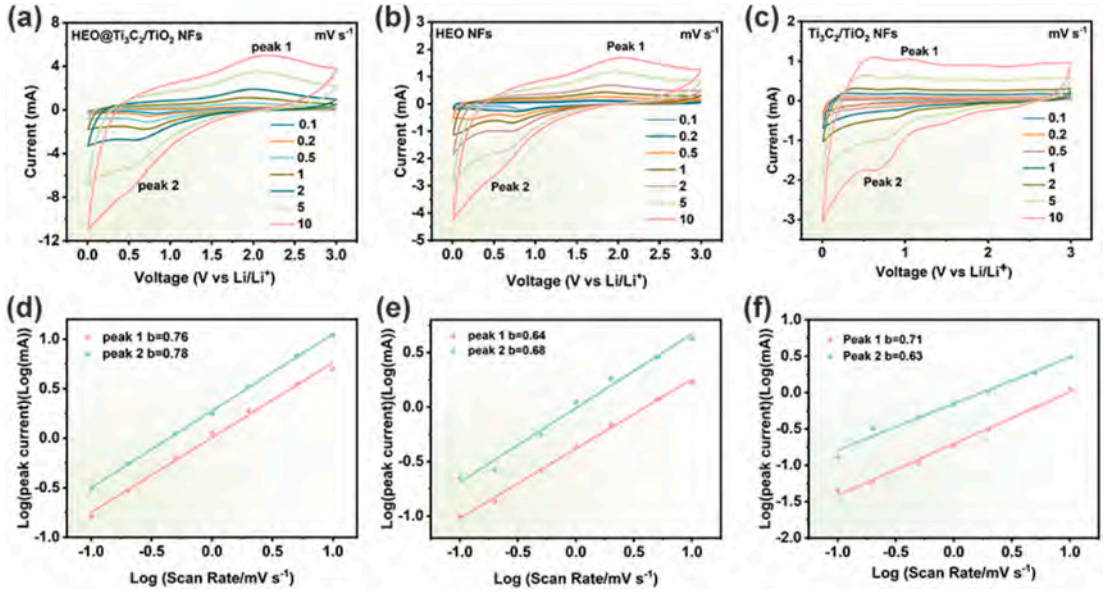

Fig. 5. (a-c) Cyclic voltammograms curves of HEO@Ti_3C_2/TiO_2 NFs, HEO NFs, and Ti_3C_2/TiO_2 NFs electrodes from 0.1 mV s^{-1} to 10 mV s^{-1}; (d-f) linear fits applied to the dependence of peak current on scanning rates.

on HEO exhibit a unique capacity change pattern, first decreasing and subsequently increasing. In the initial cycle stage, some metallic elements in the HEO are released from the lattice due to reduction reactions, resulting in a decrease in the number of active sites with a consequent decline in capacity. As the cycling process progresses, there is a regeneration of active sites through redistribution and structural reconstruction, causing the capacity to gradually recover. This phenomenon is consistent with the electrochemical behavior of HEO-based materials reported in the literature [51–54]. After 80 cycles, the specific capacity of HEO@Ti_3C_2/TiO_2 NFs reached 1330.7 mAh g^{-1}, significantly higher than that of pure HEO NF (955.9 mAh g^{-1}). At a high current density (2 A g^{-1}), the composite material retains a high specific capacity (305.9 mAh g^{-1}) after 1000 cycles, in contrast to the pure HEO NFs, which exhibits a specific capacity of 139.8 mAh g^{-1} (Fig. 4e). This result demonstrates that the incorporation of Ti_3C_2/TiO_2 significantly enhances the electrochemical performance of the electrode, outperforming most HEO anodes reported in the literature (Table S2). We have conducted kinetic studies by combining electrochemical impedance spectroscopy (EIS) and the galvanostatic intermittent titration technique (GITT). The EIS results (Fig. 4f) have established that the charge transfer resistance (R_{ct}) of HEO@Ti_3C_2/TiO_2 NFs is 33.1 Ω, which is significantly lower than that of pure HEO NFs (41.2 Ω) and pure Ti_3C_2/TiO_2 NFs (50.2 Ω). This is attributed to the continuous conductive network associated with the two-dimensional Ti_3C_2/TiO_2 structure and the strong interfacial coupling effect with HEO that effectively reduces resistance to charge transfer. The GITT curves further confirm that the Li^+ diffusion coefficient (D_{Li}^+) for this composite material is significantly enhanced (Fig. 4g), indicating that MXene promotes ion transport kinetics.

Analyses of the EIS (Fig. S11a) and GITT (Fig. S11b) data have revealed the dynamic mechanism of capacity evolution. In the initial cycling (1–50 cycles), the R_{ct} sharply increases from 33.1 Ω to 110.0 Ω, accompanied by a decrease in D_{Li}^+, which is closely related to the increase in impedance due to the formation of the SEI membrane and interfacial side reactions. In the activation stage (50–150 cycles), the R_{ct} gradually decreases to 47.5 Ω, and D_{Li}^+ first decreases and subsequently increases, indicating that the electrochemical cycling facilitates exposure of active sites with the stabilization of the interfacial passivation layer. Analysis of the CV curves (Fig. S12) supports these conclusions. In going from the pristine electrode to the 2nd cycle and then to the 50th cycle, the intensities of the anodic and cathodic peaks in the CV curves show a gradual decrease, reflecting the shift of capacity contribution from Faradaic to non-Faradaic reactions. During the stage of capacity increase, the intensities of the anodic and cathodic peaks significantly increase and the peak positions return to the levels observed in the first charge-discharge process. This suggests that the inactive elements in the early stage participate in the electrochemical reactions, and Faradaic capacity governs battery performance. The initial capacity decay is essentially a process of element redistribution and structural reconstruction accompanied by a decrease in Faradaic capacitance, where subsequent capacity increase is the result of continuous activation of Li^+ storage sites and optimization of reaction kinetics.

In order to assess the electrochemical response associated with the electrode surface and subsurface regions, the CV analysis was conducted at scan rates ranging from 0.1 to 10.0 mV s^{-1} (Fig. 5a-c). As the scan rate was increased, the peak current gradually increased. The shape of the redox curves is unaffected, demonstrating a high level of electrochemical stability. The relationship between the peak current (i_p) and scanning rate (v) abides by the formulas as follow [23]:

$$i_p = av^b \tag{1}$$

$$\log(i_p) = b\log(v) + \log(a) \tag{2}$$

where a represents a constant and b is the slope. The lithium storage mechanism of the electrode may be inferred from the value of b:b = 0.5 indicates a diffusion-controlled process, b = 1 represents pseudocapacitive control, and a b value between 0.5 and 1 implies combined diffusion and pseudocapacitance control. As shown in Fig. 5d-f, the b values of the HEO@Ti_3C_2/TiO_2 NFs electrodes are 0.76 (anode) and 0.78 (cathode), which are significantly higher than those obtained for the pure HEO NFs (0.64/0.68) and pure Ti_3C_2/TiO_2 NFs (0.71/0.63). The b values of all electrodes fall within the 0.5–1 interval, confirming that lithium storage was synergistically regulated by diffusion and pseudocapacitance. It should be noted that the b value of the composite materials is higher than pure HEO, indicating that the introduction of Ti_3C_2/TiO_2 significantly enhances the pseudocapacitance contribution. This can be attributed to the synergistic interaction between MXene nanosheets and HEO nanoparticles, where MXene forms a conductive network that facilitates electron transport. The abundant surface functional groups (*e.g.*, —O, —F) generate additional electrically active sites that contribute to a fast Faraday reaction [55].

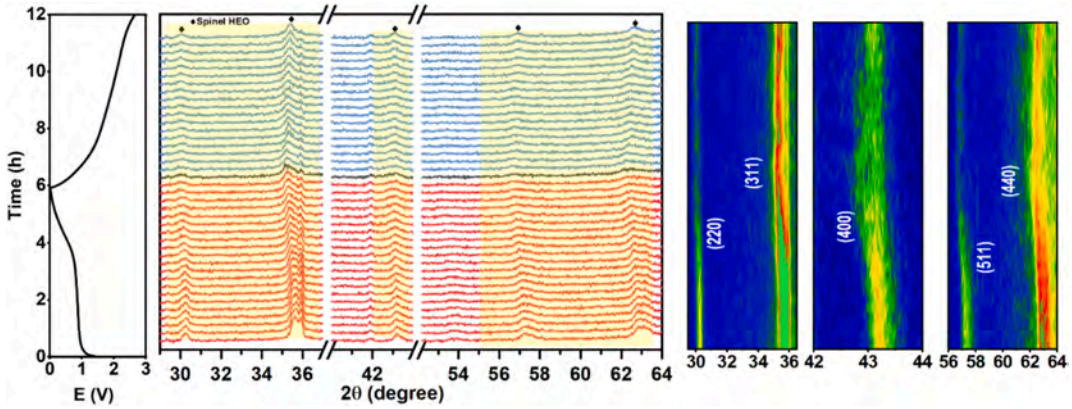

Fig. 6. *In situ* XRD patterns of the HEO@Ti_3C_2/TiO_2 NFs electrode recorded during a discharging-charging cycle.

The phase transformation of the HEO@Ti_3C_2/TiO_2 NFs materials during electrochemical cycling was evaluated by *in situ* X-ray diffraction analysis. The diffraction patterns of the HEO@Ti_3C_2/TiO_2 NFs electrode during the first charging/discharging cycle are shown in Fig. 6. The peaks at 30.28°, 35.69°, 43.34°, 57.42°, and 63.08° correspond to the (220), (311), (400), (511), and (440) planes of the spinel HEO (89-4927), respectively. During the initial discharge, there is a clear shift in the peaks due to the (220), (311), (400), (511), and (440) planes to lower angles, suggesting a lattice expansion associated with lithium insertion. Subsequently, as lithium is extracted, the peaks are shifted back to the original positions. However, an incomplete recovery of peak positions indicates that a component of active materials fails to return to the initial oxidation states following delithiation, leading to a lower Coulombic efficiency [23,52]. During the charging/discharging cycles, the XRD peaks associated with the HEO spinel structure gradually diminish but are still detectable, suggesting that the HEO nanocrystals are retained. This phenomenon may be ascribed to the lower rigidity of the HEO lattice, where certain metal elements play a crucial role in maintaining overall structural stability. This characteristic enables a more flexible rearrangement of atoms during lithiation/delithiation, ultimately resulting in enhanced electrochemical reversibility [56,57].

The HEO@Ti_3C_2/TiO_2 NFs deliver superior electrochemical performance, notably the highest discharging specific capacity, optimal rate capability, and cycling stability. This response can be attributed to several factors:

(i) Anchoring HEO nanoparticles to the Ti_3C_2/TiO_2 surface generates a strong interfacial coupling, which enhances charge transfer and promotes effective Li^+ storage.
(ii) The nanofibers exhibit a high specific surface area and abundant active sites. The synergistic interaction between the HEO and Ti_3C_2/TiO_2 establishes a robust conductive pathway that enhances electrical conductivity.
(iii) The physicochemical reactions associated with HEO nanoparticles are highly complex. During the rapid extraction and insertion of lithium ions, the spinel lattice, offering stable channels for Li^+ diffusion and preserving material structural integrity, is consistently present. This feature ensures highly reversible lithium storage.

3. Conclusions

In this work, HEO@Ti_3C_2/TiO_2 NFs composites were successfully synthesized by an electrostatic spinning and stepwise annealing process. The Ti_3C_2/TiO_2 nanosheets were combined with HEO nanofibers through interfacial engineering to construct a three-dimensional conductive network, introducing oxygen vacancies that reduced charge transfer resistance. The Ti_3C_2/TiO_2-based or HEO-based materials can serve as a new platform for the design of high-performance energy storage electrode materials with potential applications in systems such as sodium-ion and zinc-ion batteries.

CRediT authorship contribution statement

Yingying Lu: Data curation, Writing – original draft. **Yi Zhang:** Data curation. **Hailong Yan:** Methodology. **Jinbing Cheng:** Resources. **Yongsong Luo:** Funding acquisition. **Paul K. Chu:** Writing – review & editing.

Declaration of competing interest

The authors declare no conflict of interest.

Acknowledgments

This work was financially supported by the National Natural Science Foundation of China (52272219), Natural Science Foundation of Henan Province (242300421191), Collaborative Innovation Center of Intelligent Explosion-proof Equipment of Henan Province, as well as City University of Hong Kong Donation Research Grants (DON-RMG No. 9229021 and No. 9220061).

Appendix A. Supplementary data

Supplementary data to this article can be found online at https://doi.org/10.1016/j.cej.2025.165230.

Data availability

Data will be made available on request.

References

[1] W. Yan, Z. Mu, Z. Wang, Y. Huang, D. Wu, P. Lu, J. Lu, J. Xu, Y. Wu, T. Ma, M. Yang, X. Zhu, Y. Xia, S. Shi, L. Chen, H. Li, F. Wu, Hard-carbon-stabilized Li-Si anodes for high-performance all-solid-state Li-ion batteries, Nat. Energy 8 (2023) 800–813.
[2] Z. Li, I. Sami, J. Yang, J. Li, R.V. Kumar, M. Chhowalla, Lithiated metallic molybdenum disulfide nanosheets for high-performance lithium-sulfur batteries, Nat. Energy 8 (2023) 84–93.
[3] J. Chen, Y. Xu, Y. Wang, Z. Lv, S. Zhang, W. Dong, J. Hou, Y. Fang, H. Bi, F. Huang, Molecular key tuned steric-hindrance effect toward Zn (100) facet texture anode, Energy Storage Mater. 72 (2024) 103765.
[4] W. Kim, D. Shin, B. Seo, S. Chae, E. Jo, W. Choi, Precisely tunable synthesis of binder-free cobalt oxide-based Li-ion battery anode using scalable electrothermal waves, ACS Nano 16 (2022) 17313–17325.
[5] H. Li, M.B. Kaleem, K. Liu, Y. Wu, W. Liu, Q. Peng, Fault prognosis of Li-ion batteries in electric vehicles: recent progress, challenges and prospects, J. Energy Storage 116 (2025) 116002.

[6] K. Xu, X. Li, X. Liu, Y. Yu, X. Zhang, W. Lei, Z. Xie, S. Zhang, Q. Jia, H. Zhang, In-situ synthesis of Si@G@TiC double protective layer structure for enhancing cycling stability of lithium-ion batteries, Sustain. Mater. Technol. 36 (2023) e00583.

[7] Y. Chen, Y. Zou, X. Shen, J. Qiu, J. Lian, J. Pu, S. Li, F. Du, S. Li, Z. Ji, A. Yuan, Ge nanoparticles uniformly immobilized on 3D interconnected porous graphene frameworks as anodes for high-performance lithium-ion batteries, J. Energy Chem. 69 (2022) 161–173.

[8] H.G. Nam, J.Y. Park, J.M. Yuk, S.M. Han, Phase transformation mechanism and stress evolution in Sn anode, Energy Storage Mater. 45 (2022) 101–109.

[9] J. Li, S. Hwang, F. Guo, S. Li, Z. Chen, R. Kou, K. Sun, C. Sun, H. Gan, A. Yu, E. A. Stach, H. Zhou, D. Su, Phase evolution of conversion-type electrode for lithium-ion batteries, Nat. Commun. 10 (2019) 2224.

[10] X. Yan, H. Kang, P. Cheng, S. Zhang, S. Shi, W. Liu, Monolithic three-dimensional hollow nanoporous Cu_xO encapsulated mesoporous Cu heterostructures with superior Li storage properties, EcoMat 4 (2022) e12208.

[11] S. Park, B. Seo, D. Shin, S. Chae, H. Cho, S. Kim, W. Choi, Synthesis of carbon nanotube-iron oxide composites via combustion waves for hybrid Li-ion battery anodes, Chem. Eng. J. 470 (2023) 144260.

[12] I.W.M. Smith, Laboratory astrochemistry: gas-phase processes, Annu. Rev. Astron. Astrophys. 49 (2011) 29–66.

[13] C.-L. Zhang, S.-H. Yu, Nanoparticles meet electrospinning: recent advances and future prospects, Chem. Soc. Rev. 43 (2024) 4423–4448.

[14] H. Liu, Y. Zhu, C. Zhang, Y. Zhou, D.-G. Yu, Electrospun nanofiber as building blocks for high-performance air filter: a review, Nano Today 55 (2024) 102161.

[15] Q. Liu, J. Zhu, L. Zhang, Y. Qiu, Recent advances in energy materials by electrospinning, Renew. Sust. Energ. Rev. 81 (2018) 1825–1858.

[16] T.X. Nguyen, J. Patra, J.-K. Chang, J.-M. Ting, High entropy spinel oxide nanoparticles for superior lithiation-delithiation performance, J. Mater. Chem. A 8 (2020) 18963–18973.

[17] J.-Z. Yen, Y.-C. Yang, H.-Y. Tuan, Interface engineering of high entropy oxide@polyaniline heterojunction enables highly stable and excellent lithium ion storage performance, Chem. Eng. J. 450 (2022) 137924.

[18] A. Sarkar, L. Velasco, D. Wang, Q. Wang, G. Talasila, L. de Biasi, C. Kübel, T. Brezesinski, S.S. Bhattacharya, H. Hahn, B. Breitung, High entropy oxides for reversible energy storage, Nat. Commun. 9 (2018) 3400.

[19] D. Wang, Z. Liu, S. Du, Y. Zhang, H. Li, Z. Xiao, W. Chen, R. Chen, Y. Wang, Y. Zou, S. Wang, Low-temperature synthesis of small-sized high-entropy oxides for water oxidation, J. Mater. Chem. A 7 (2019) 24211–24216.

[20] D. Shin, S. Chae, S. Park, B. Seo, W. Choi, Rational engineering of high-entropy oxides for Li-ion battery anodes with finely tuned combustion syntheses, NPG Asia Mater. 15 (2023) 54.

[21] C. Triolo, M. Maisuradze, M. Li, Y. Liu, A. Ponti, G. Pagot, V. Di Noto, G. Aquilanti, N. Pinna, M. Giorgetti, S. Santangelo, Charge storage mechanism in electrospun spinel-structured high-entropy $(Mn_{0.2}Fe_{0.2}Co_{0.2}Ni_{0.2}Zn_{0.2})_3O_4$ oxide nanofibers as anode material for Li-ion batteries, Small 19 (2023) 2304585.

[22] X.L. Wang, E.M. Kim, T.G. Senthamaraikannan, D.-H. Lim, S.M. Jeong, Porous hollow high entropy metal oxides $(NiCoCuFeMg)_3O_4$ nanofiber anode for high-performance lithium-ion batteries, Chem. Eng. J. 484 (2024) 149509.

[23] X. Liu, Y. Yu, K. Li, Y. Li, X. Li, Z. Yuan, H. Li, H. Zhang, M. Gong, W. Xia, Y. Deng, W. Lei, Intergrating hollow multishelled structure and high entropy engineering toward enhanced mechano-electrochemical properties in lithium battery, Adv. Mater. 36 (2024) 2312583.

[24] W. Chen, A. Hilhorst, G. Bokas, S. Gorsse, P.J. Jacques, G. Hautier, A map of single-phase high-entropy alloys, Nat. Commun. 14 (2023) 2856.

[25] F.Y. Zhai, P.Y. Yang, W.F. Zhang, X.Y. Zhu, G.P. Cao, H.M. Zhang, Y.L. Xing, Y. P. Lei, Y. Xiang, S.C. Zhang, Creative high-entropy strategy: a booster to the design of anode materials for high-energy lithium-ion batteries, Rare Metals (2025), https://doi.org/10.1007/s12598-025-03309-8.

[26] C.E. Park, R.A. Senthil, G.H. Jeong, M.Y. Choi, Architecting the high-entropy oxides on 2D MXene nanosheets by rapid microwave-heating strategy with robust Photoelectrochemical oxygen evolution performance, Small 19 (27) (2023) 2207820.

[27] T. Li, Y. Yao, B.H. Ko, Z. Huang, Q. Dong, J. Gao, W. Chen, J. Li, S. Li, X. Wang, R. Shahbazian-Yassar, F. Jiao, L. Hu, Carbon-supported high-entropy oxide nanoparticles as stable electrocatalysts for oxygen reduction reactions, Adv. Funct. Mater. 31 (2021) 2010561.

[28] R. Jia, R. Yang, Y. Zheng, Q. Pan, F. Zhang, Y. Tang, Anomalous electrochemical aging strengthening behavior of MXene electrodes for synergistic anion-cation storage in dual-ion batteries, Adv. Funct. Mater. 35 (2025) 2419013.

[29] D. Johnson, Z. Qiao, E. Uwadiunor, A. Uwadiunor, Holdups in nitride MXene's development and limitations in advancing the field of MXene, Small 18 (2022) 2106129.

[30] G. Murali, J.K. Reddy Modigunta, Y.H. Park, J.-H. Lee, J. Rawal, S.-Y. Lee, I. In, S.-J. Park, A review on MXene synthesis, stability, and photocatalytic applications, ACS Nano 16 (2022) 13370–13429.

[31] M. Tian, J. Lyu, R. Su, X. Zhang, K. Wang, X. Lv, D. Zhang, S.W. Yang, J.H.K. Yip, Z. Hao, G.Q. Xu, Harnessing the power of nano-ferroelectrics: $BaTiO_3$/MXene ($Ti_3C_2T_x$) composites for enhanced lithium storage, Adv. Energy Mater. 14 (2024) 2401988.

[32] Z. Yang, C. Weng, X. Gao, F. Meng, Y. Ji, J. Li, T. Lu, J. Li, J. Wang, L. Pan, In situ construction of Sn-based metal-organic frameworks on MXene achieving fast electron transfer for rapid lithium storage, Chem. Eng. J. 486 (2024) 150299.

[33] S. Zhou, L. Jiang, H. Wang, J. Yang, X. Yuan, H. Wang, J. Liang, X. Li, H. Li, Y. Bu, Oxygen vacancies modified TiO_2/O-terminated Ti_3C_2 composites: unravelling the dual effects between oxygen vacancy and high-work-function titanium carbide, Adv. Funct. Mater. 33 (2023) 2307702.

[34] A.S. Levitt, M. Alhabeb, C.B. Hatter, A. Sarycheva, G. Dion, Y. Gogotsi, Electrospun MXene/carbon nanofibers as supercapacitor electrodes, J. Mater. Chem. A 7 (2019) 269–277.

[35] F. Qi, L. Shao, X. Lu, G. Liu, X. Shi, Z. Sun, MXene-derived $TiSe_2/TiO_2/C$ heterostructured hexagonal prisms as high rate anodes for Na-ion and K-ion batteries, Appl. Surf. Sci. 605 (2022) 154653.

[36] Y. Guo, D. Zhang, Z. Bai, Y. Yang, Y. Wang, J. Cheng, P.K. Chu, Y. Luo, MXene nanofibers confining MnOx nanoparticles: a flexible anode for high-speed lithium ion storage networks, Dalton Trans. 51 (2022) 1423–1433.

[37] L. Zhang, S. Xia, X. Zhang, Y. Yao, Y. Zhang, S. Chen, Y. Chen, J. Yan, Low-temperature synthesis of mesoporous half-metallic high-entropy spinel oxide nanofibers for photocatalytic CO_2 reduction, ACS Nano 18 (2024) 5322–5334.

[38] C. Triolo, S. Schweidler, L. Lin, G. Pagot, V. Di Noto, B. Breitung, S. Santangelo, Evaluation of electrospun spinel-type high-entropy $(Cr_{0.2}Mn_{0.2}Fe_{0.2}Co_{0.2}Ni_{0.2})_3O_4$, $(Cr_{0.2}Mn_{0.2}Fe_{0.2}Co_{0.2}Zn_{0.2})_3O_4$ and $(Cr_{0.2}Mn_{0.2}Fe_{0.2}Ni_{0.2}Zn_{0.2})_3O_4$ oxide nanofibers as electrocatalysts for oxygen evolution in alkaline medium, Energy Adv. 2 (2023) 667–678.

[39] K. Du, Y. Liu, Y. Yang, F. Cui, J. Wang, M. Han, J. Su, J. Wang, X. Han, Y. Hu, High entropy oxides modulate atomic-level interactions for high-performance aqueous zinc-ion batteries, Adv. Mater. 35 (2023) 2301538.

[40] B. Petrovićovà, W. Xu, M.G. Musolino, F. Pantò, S. Patanè, N. Pinna, S. Santangelo, C. Triolo, High-entropy spinel oxides produced via sol-gel and electrospinning and their evaluation as anodes in Li-ion batteries, Appl. Sci. 12 (2022) 5965.

[41] K.-H. Tian, C.-Q. Duan, Q. Ma, X.-L. Li, Z.-Y. Wang, H.-Y. Sun, S.-H. Luo, D. Wang, Y.-G. Liu, High-entropy chemistry stabilizing spinel oxide $(CoNiZnXMnLi)_3O_4$ (X = Fe, Cr) for high-performance anode of Li-ion batteries, Rare Metals 41 (2021) 1265–1275.

[42] Y. Wu, Z. Zhu, Y. Li, D. Shen, L. Chen, T. Kang, X. Lin, Z. Tong, H. Wang, C.S. Lee, Aqueous MnV_2O_6-Zn battery with high operating voltage and energy density, Small 17 (2021) 2008182.

[43] B. Xiao, G. Wu, T. Wang, Z. Wei, Y. Sui, B. Shen, J. Qi, F. Wei, J. Zheng, High-entropy oxides as advanced anode materials for long-life lithium-ion batteries, Nano Energy 95 (2022) 106962.

[44] P. Ghigna, L. Airoldi, M. Fracchia, D. Callegari, U. Anselmi-Tamburini, P. D'Angelo, N. Pianta, R. Ruffo, G. Cibin, D.O. de Souza, E. Quartarone, Lithiation mechanism in high-entropy oxides as anode materials for Li-ion batteries: an operando XAS study, ACS Appl. Mater. Interfaces 12 (2020) 50344–50354.

[45] C.-Y. Huang, C.-W. Huang, M.-C. Wu, J. Patra, T. Xuyen Nguyen, M.-T. Chang, O. Clemens, J.-M. Ting, J. Li, J.-K. Chang, W.-W. Wu, Atomic-scale investigation of lithiation/delithiation mechanism in high-entropy spinel oxide with superior electrochemical performance, Chem. Eng. J. 420 (2021) 129838.

[46] W. Li, Y. Li, J.-H. Wang, S. Huang, A. Chen, L. Yang, J. Chen, L. He, W.K. Pang, L. Thomsen, B. Cowie, P. Xiong, Y. Zhou, G. Jang, D.H. Min, J.S. Byun, L. Xu, J.-Q. Huang, K.C. Roh, S.H. Kang, M. Liu, X. Duan, H.S. Park, Generic synthesis of high-entropy phosphides for fast and stable Li-ion storage, Energy Environ. Sci. 17 (2024) 5387–5398.

[47] N. Liu, Q. Li, H. Wan, L. Chang, H. Wang, J. Fang, T. Ding, Q. Wen, L. Zhou, X. Xiao, High-temperature stability in air of $Ti_3C_2T_x$ MXene-based composite with extracted bentonite, Nat. Commun. 13 (2022) 5551.

[48] C. Lu, X. Li, R. Liu, H.J. Niu, Q. Wang, T. Xiao, J. Liu, H. Wang, W. Zhou, Optimized Ti-O subcompounds and elastic expanded MXene interlayers boost quick sodium storage performance, Adv. Funct. Mater. 33 (2023) 2215228.

[49] X. Liu, Y. Xing, K. Xu, H. Zhang, M. Gong, Q. Jia, S. Zhang, W. Lei, Kinetically accelerated lithium storage in high-entropy (LiMgCoNiCuZn)O enabled by oxygen vacancies, Small 18 (2022) 2200524.

[50] X. Liu, X. Li, Y. Li, H. Zhang, Q. Jia, S. Zhang, W. Lei, High-entropy oxide: a future anode contender for lithium-ion battery, EcoMat 4 (2022) e12261.

[51] N. Ci, Y. Hu, Q. Li, J. Cheng, H. Zhang, D. Li, K. Li, K.M. Reddy, L. Ci, G. Xie, X. Liu, H.J. Qiu, Cycling reconstructed hierarchical nanoporous high-entropy oxides with continuously increasing capacity for Li storage, Small Methods 8 (2024) 2301322.

[52] S. Zhu, W. Nong, L.J.J. Nicholas, X. Cao, P. Zhang, Y. Lu, M. Xiu, K. Huang, G. Wu, S.-W. Yang, J. Wu, Z. Liu, M. Srinivasan, K. Hippalgaonkar, Y. Huang, Rapid in situ growth of high-entropy oxide nanoparticles with reversible spinel structures for efficient Li storage, J. Mater. Chem. A 12 (2024) 11473–11486.

[53] X. Liu, R. Tao, C. Li, J. Wang, S. Yao, C. Hong, H. Li, J. Geng, J. Liang, Inert salt-assisted solvent-free synthesis of high-entropy oxide towards high-performance lithium-ion batteries, Chem. Eng. J. 184 (2024) 149791.

[54] L. Su, J. Ren, T. Lu, K. Chen, J. Ouyang, Y. Zhang, X. Zhu, L. Wang, H. Min, W. Luo, Z. Sun, Q. Zhang, Y. Wu, L. Sun, L. Mai, F. Xu, Deciphering structural origins of highly reversible lithium storage in high entropy oxides with in situ transmission electron microscopy, Adv. Mater. 35 (2023) 2205751.

[55] X. Han, Q. Meng, X. Wan, B. Sun, Y. Zhang, B. Shen, J. Gao, Y. Ma, P. Zuo, S. Lou, G. Yin, Intercalation pseudocapacitive electrochemistry of Nb-based oxides for fast charging of lithium-ion batteries, Nano Energy 81 (2021) 105635.

[56] S. Hou, L. Su, S. Wang, Y. Cui, J. Cao, H. Min, J. Bao, Y. Shen, Q. Zhang, Z. Sun, C. Zhu, J. Chen, Q. Zhang, F. Xu, Unlocking the origins of highly reversible lithium storage and stable cycling in a spinel high-entropy oxide anode for lithium-ion batteries, Adv. Funct. Mater. 34 (2024) 2307923.

[57] K. Wang, W. Hua, X. Huang, D. Stenzel, J. Wang, Z. Ding, Y. Cui, Q. Wang, H. Ehrenberg, B. Breitung, C. Kübel, X. Mu, Synergy of cations in high entropy oxide lithium ion battery anode, Nat. Commun. 14 (2023) 1487.

Supporting Information

Integration of Ti_3C_2/TiO_2 and spinel high-entropy oxide: A novel strategy for enhancing lithium-ion battery performance

Yingying Lu [1], Yi Zhang [1], Hailong Yan [1,*], Paul K. Chu [2], Jinbing Cheng [1,*], and Yongsong Luo [1,*]

[1] Henan International Joint Laboratory of MXene Materials Microstructure, Nanyang Normal University, Nanyang 473061, China

[2] Department of Physics, Department of Materials Science & Engineering, and Department of Biomedical Engineering, City University of Hong Kong, Tat Chee Avenue, Kowloon, Hong Kong, China

[*]Corresponding authors: yanhailong2005@126.com (H.L. Yan); chengjinbing1988@163.com (J.B. Cheng); eysluo@163.com (Y.S. Luo)

1. Experimental Section

1.1. Materials

$Cu(CH_3COO)_2 \cdot H_2O$ (0.4 mmol), $Mn(CH_3COO)_2 \cdot 4H_2O$ (0.4 mmol), $Ni(CH_3COO)_2 \cdot 4H_2O$ (0.4 mmol), $Co(CH_3COO)_2$ (0.4 mmol), $Zn(CH_3COO)_2$ (0.4 mmol), $Fe(NO_3)_3 \cdot 9H_2O$ (0.4 mmol), N, N-dimethylformamide (DMF, 99.5%), polyacrylonitrile (PAN, 250,000).

1.2. Preparation of MXene

The preparation of MXene began with the addition of 1 g of lithium fluoride to 30 ml of 9 mol L^{-1} hydrochloric acid at room temperature and stirring until the solution became clear. Subsequently, 40% hydrofluoric acid (9 mL) was added and stirred for 10 minutes, and 1 g of Ti_3AlC_2 powder was added gradually during the course of 1 hour. The solution was then stirred at 37 °C for 10 hours to etch aluminum from Ti_3AlC_2 by hydrofluoric acid, centrifuged at 5,500 rpm until reaching a neutral pH, and aspirated with argon for 30 minutes at a temperature not exceeding 25 °C. The resulting Ti_3C_2 MXene solution was transferred to a beaker and sonicated for 1 hour at a low temperature. Additional centrifugation was carried out at 3,500 rpm and 8,000 rpm for 1 hour each to yield the Ti_3C_2 MXene colloid. The Ti_3C_2 MXene colloid was dispersed in dimethylformamide (DMF) and sonicated for 1.5 hours at a low temperature to obtain a homogeneous Ti_3C_2 MXene solution (40 mg mL^{-1}), with careful attention to maintain the temperature to not exceed 25 °C throughout the process.

1.3. Preparation of HEO@Ti_3C_2/TiO_2 NFs

First, 2 mL of Ti_3C_2 MXene dispersion and the above six metal salts were added to 8 mL of DMF and stirred for 10 min, followed by sonication in ice water for 10 min, and this operation was repeated three times to obtain a homogeneous dispersion. Subsequently, 1 g PAN was added and stirred for 8 h to prepare the precursor solution. Electrospinning was performed to obtain pristine carbon nanofibers at a solution flow rate of 0.5 mL h^{-1} with a distance of 13 cm between the collecting and receiving rollers and a voltage of 24.0 kV. The collected nanofibers were dried at 60 °C for 8 h and then pre-oxidized in air at 250 °C (2 °C min^{-1}) for 30 min to stabilize the structure of the nanofibers. The nanofibers were calcined in air at 500 °C for 30 min (10 °C min^{-1}) to obtain high entropy HEO@Ti_3C_2/TiO_2 NFs.

1.4. Synthesis of HEO NFs and Ti_3C_2/TiO_2 NFs

As a control, HEO NFs and Ti_3C_2/TiO_2 NFs were prepared. Control samples of HEO NFs were prepared in the same manner as the HEO NFs but without the addition of Ti_3C_2 MXene. Similarly, Ti_3C_2/TiO_2 NFs were prepared without the addition of metal salts.

2. Material characterization

The crystal structure was determined by X-ray diffraction instrument (XRD, Rigaku D/texultra 250) with Cu K_α radiation in the 2θ angle range of 5° to 80° at a rate of 10°·min^{-1} and step size of 0.02°. The Raman spectra were recorded on the Raman

microprobe (Renishaw instrument) with a 532 nm laser and 50x objective lens. The morphology and grain size of the precursor fibers and fibers after calcination were observed by field-emission scanning electron microscopy (FE-SEM, Sigma 500, German) and transmission electron microscopy (TEM, JEOL JEM F200, Japan), respectively. The elemental distribution was determined by energy-dispersive X-ray spectroscopy (EDS, Thermo Scientific K-Alpha, USA). The element content was measured by an inductively coupled plasma optical emission spectrometry (ICP-OES, Agilent 5110) with 1.2 kW RF power. Thermogravimetric curves were recorded by a thermal analyzer (STA 449C, Netzsch) in flowing air. The relative content of oxygen vacancies was detected by an EPR spectrometer (Germany, EMXplus-6/1). N_2 adsorption/desorption isotherms were obtained by a surface area and porosity analyzer (ASAP 2460, Micromeritics, USA).

3. Battery assembly and electrochemical assessment

The properties of HEO@Ti_3C_2/TiO_2 NFs as the negative electrode in the LIB were determined using CR2032 button cells. The active materials (calcined HEO@Ti_3C_2/TiO_2 NFs), acetylene black, and polyvinylidene fluoride (PVDF) were mixed with a mass ratio of 7:2:1 and stirred continuously with N-methyl-2-pyrrolidone (NMP, Innochem) for 12 hours. The slurry was evenly coated onto a copper foil using a doctor blade device and dried for 6 hours at 80 ℃. The electrode was cut into disks with a diameter of approximately 12 mm，with each disc containing an active material loading of 1-1.2 mg cm^{-2}. The half-button cells were assembled in an Ar-filled glove

box, with a lithium metal foil as the reference electrode. The electrolyte was 1 M $LiPF_6$ in an EC/DMC/DEC (1:1:1, V/V/V), and 100 uL of the electrolyte was carefully added to each cell. The microporous polyethylene Celgard 2400 film was the separator. The constant current charging-discharging, cycling, and rate properties were determined on the multi-channel battery tester (LANDIAN CT 3001 A) at room temperature. Cyclic voltammetry (CV) and electrochemical impedance spectroscopy (EIS) were performed on an electrochemical workstation (CHI660E) in the voltage window of 0.01~3.0 V.

Table S1. ICP-OES results of the as-prepared HEO NFs.

Element	Mn	Co	Ni	Cu	Zn	Fe
Concentration (mg/kg)	110983.72	95378.24	122711.16	125772.66	105784.38	118105.23
Atomic (%)	16.36	14.04	18.07	18.52	15.59	16.75

Equation S1:

$$\Delta S_{config} = -R\left[\left(\sum_{i=1}^{N} x_i \ln x_i\right)_{cation\ site} + \left(\sum_{j=1}^{N} x_j \ln x_j\right)_{anion\ site}\right]$$

where x_i is the mole fractions of ions in cation site, the mole fractions of ions in the anion site are represented via x_j, and R represent the gas constant.

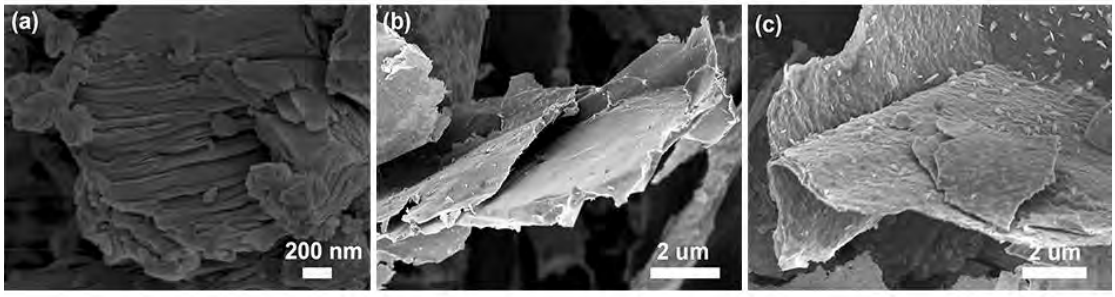

Fig. S1. SEM images of (a) Ti_3AlC_2, (b) Ti_3C_2 nanosheets, and (c) Ti_3C_2/TiO_2 nanosheets.

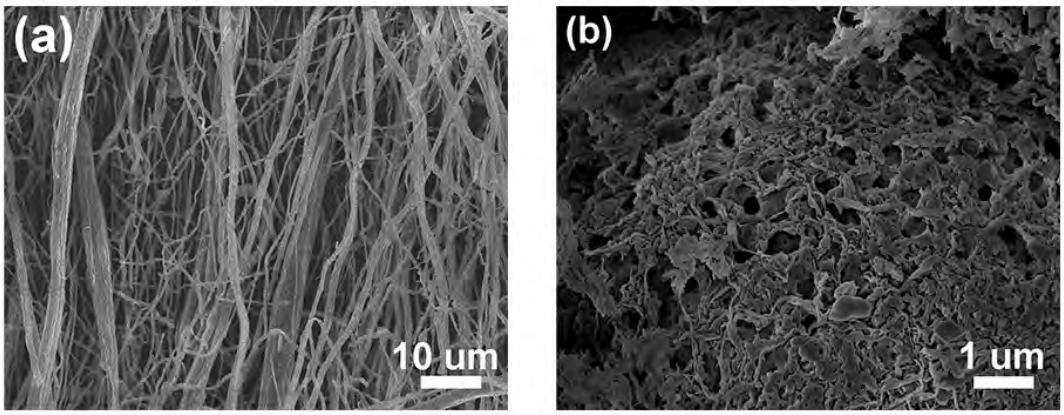

Fig. S2. SEM images of Ti_3C_2 dispersion added at (a) 1 mL and (b) 3 mL.

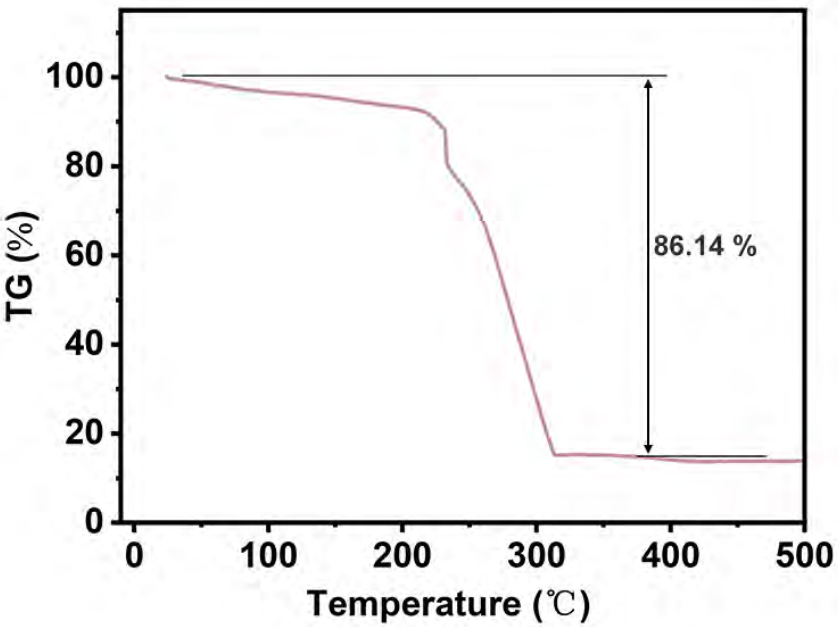

Fig. S3. TG curve of precursor (in flowing air).

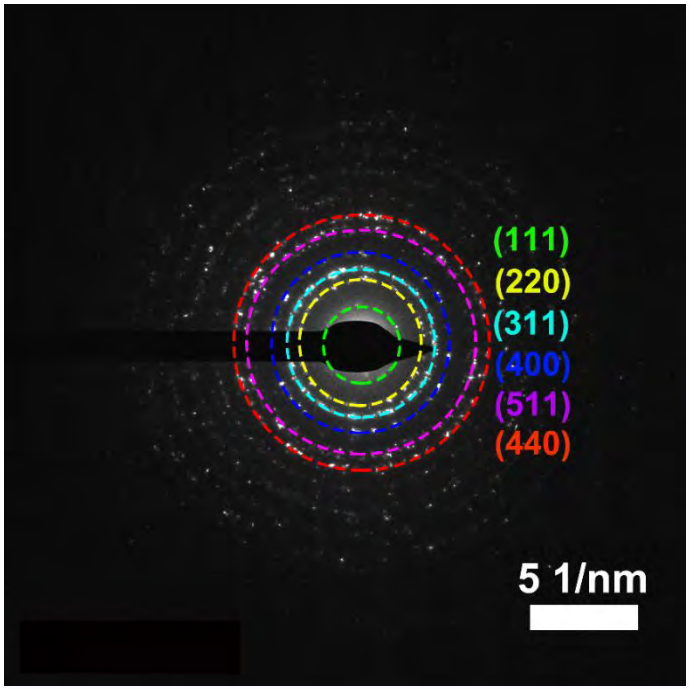

Fig. S4. SAED pattern of the relevant region.

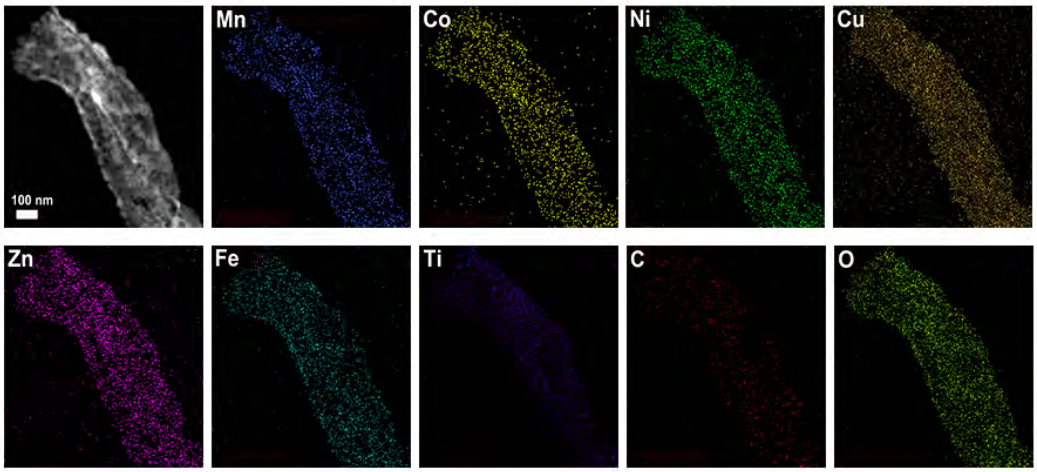

Fig. S5. EDS mappings of HEO@Ti_3C_2/TiO_2 NFs.

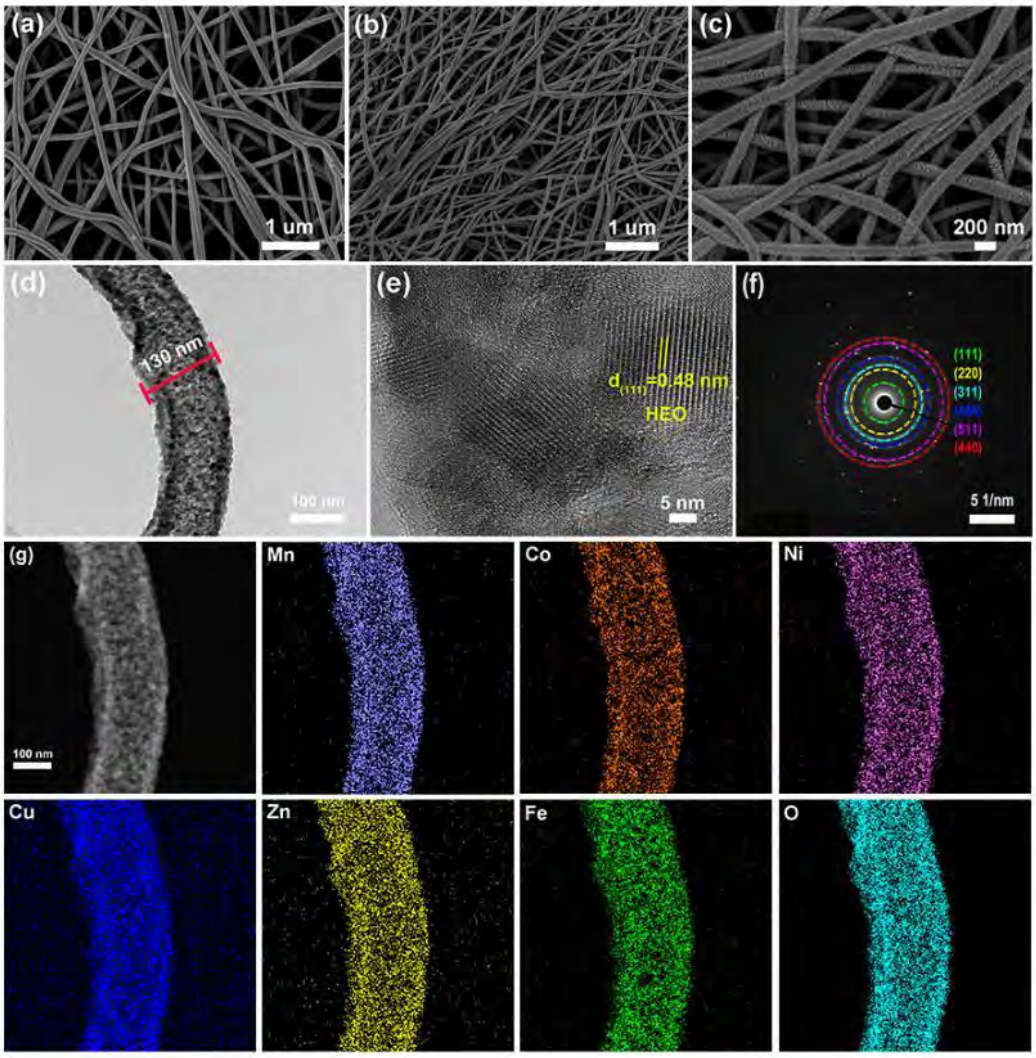

Fig. S6. (a) SEM image of primordial HEO NFs; (b-c) SEM images of HEO NFs; (d) TEM image of HEO NFs; (e) HR-TEM image of HEO NFs; (f) SAED pattern of the HEO NFs relevant region; (g) EDS mappings of HEO NFs.

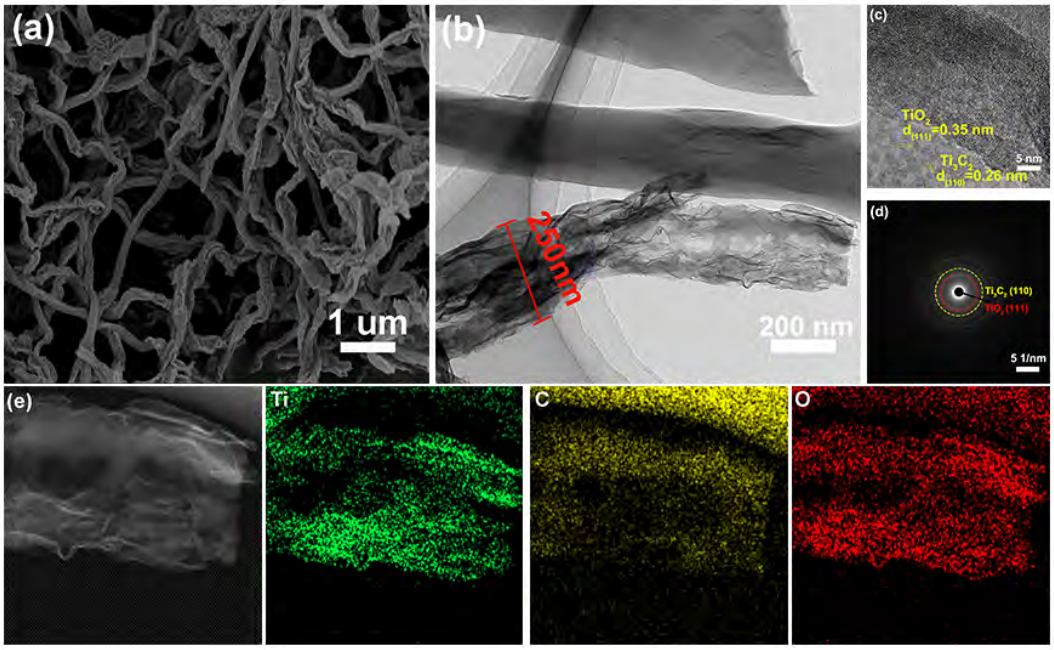

Fig. S7. (a) SEM image of Ti_3C_2/TiO_2 NFs; (b) TEM image of Ti_3C_2/TiO_2 NFs; (c) HR-TEM image of Ti_3C_2/TiO_2 NFs; (c) SAED pattern of the Ti_3C_2/TiO_2 NFs relevant region; (d) EDS mappings of Ti_3C_2/TiO_2 NFs.

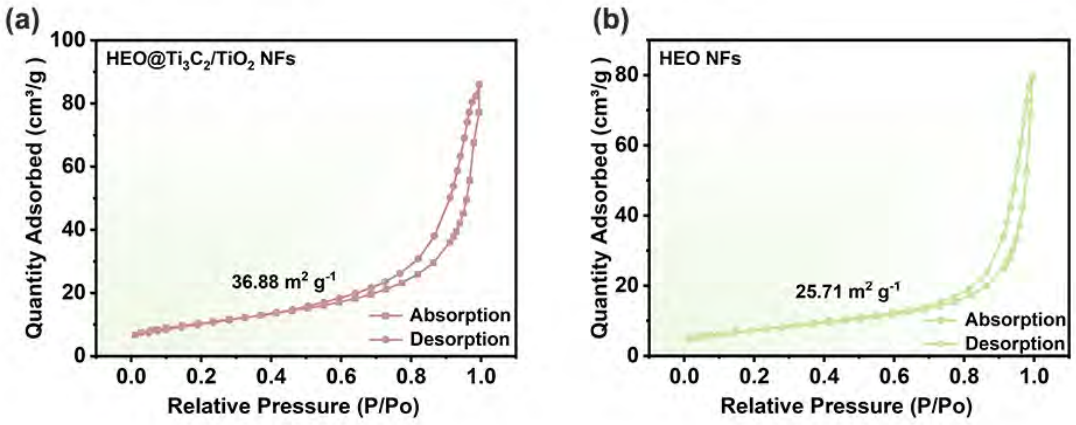

Fig. S8. N_2 adsorption-desorption curves of (a) HEO@Ti_3C_2/TiO_2 NFs and (b) HEO NFs.

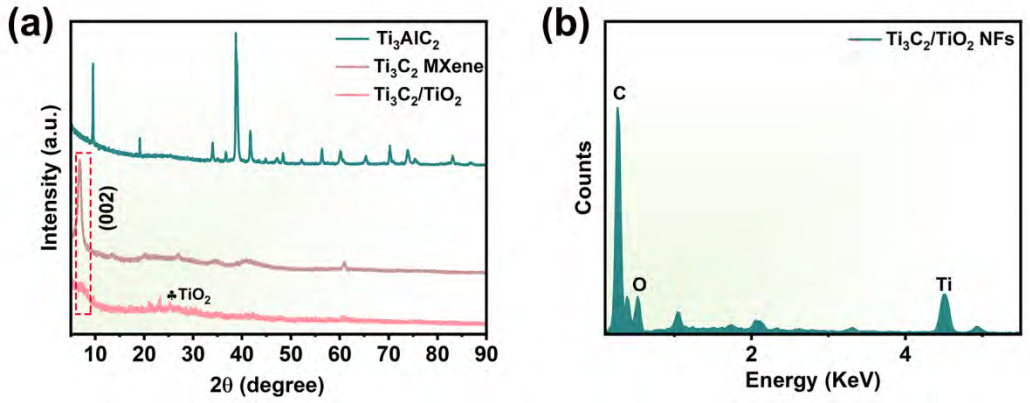

Fig. S9. (a) XRD patterns of Ti_3AlC_2, Ti_3C_2 and Ti_3C_2/TiO_2; (b) EDS analysis of Ti_3C_2/TiO_2 NFs.

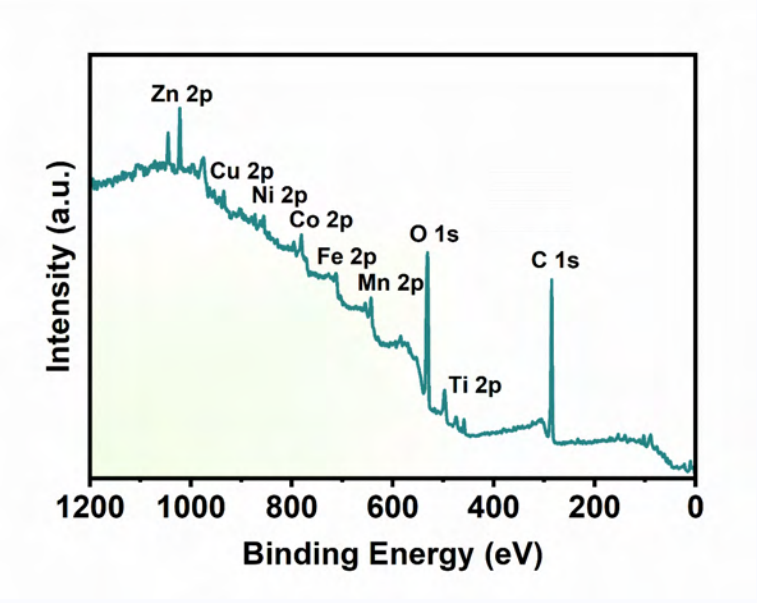

Fig. S10. XPS survey spectrum of HEO@Ti_3C_2/TiO_2 NFs.

Table S2. Recent comparative studies on the performance of HEO in the field of lithium-ion batteries.

HEO structure	Chemical composition	Capacity at 0.1 A g^{-1}/ mAh g^{-1}	Cycle performance (cycles)/mAh g^{-1}	References
Spinel	$(FeZnNiCrMn)_3O_4$	830	660 (200) at 0.5 A g^{-1}	Adv. Funct. Mater. 33 (2023) 2300509.
Spinel	$Sn_{0.8}(CoMgMnNiZn)_{2.2}O_4$	540	438 (900) at 0.5 A g^{-1}	Small (2023) 2304585.
Spinel	$La(CoCrFeMnNi)O_3$	371	569(500) at 0.2 A g^{-1}	J. Adv. Ceram. 12 (2023) 1214-1227.
Spinel	$(CrNiMnFeCu)_3O_4$	760	710(400) at 0.5 A g^{-1}	Adv. Funct. Mater. 32 (2022) 2110992.
Spinel rock-salt	$(CrMnFeCoNiZn)_3O_4$	876.5	667.3 (350) at 0.5 A g^{-1}	Compos. Part B-Eng. (2025) 112175.
Spinel rock-salt	LiF/MgCoNiMnZnO	756.3	552.2 (1000) at 0.5 A g^{-1}	J. Alloy. Compd. 986 (2024) 174140.
Spinel	$((Fe_{0.45}Co_{0.14}Ni_{0.2}Cr_{0.13}Mn_{0.08})_3O_4)$@rGO	794	530 (200) at 0.5A g^{-1}	J. Energy Storage 80 (2024) 110325.
Rock salt	(LiMgCoNiCuZn)O	714	417 (300) at 1 A g^{-1}	Small 18 (2022) 2200524.
Rock salt	(MgCoNiCuZn)O	397	390(300) at 0.5 A g^{-1}	Adv. Funct. Mater. 32 (2022) 2202892.
Rock salt	$(CoNiMgZnFe)_3O_{3.2}$	780	600 (200) at 0.1 A g^{-1}	Adv. Mater. 35 (2023) 2205751
Spinel	$(MnCoNiCuZnFe)_3O_4$@ Ti_3C_2/TiO_2	955.9	305.9 (1000) at 2 A g^{-1}	This work

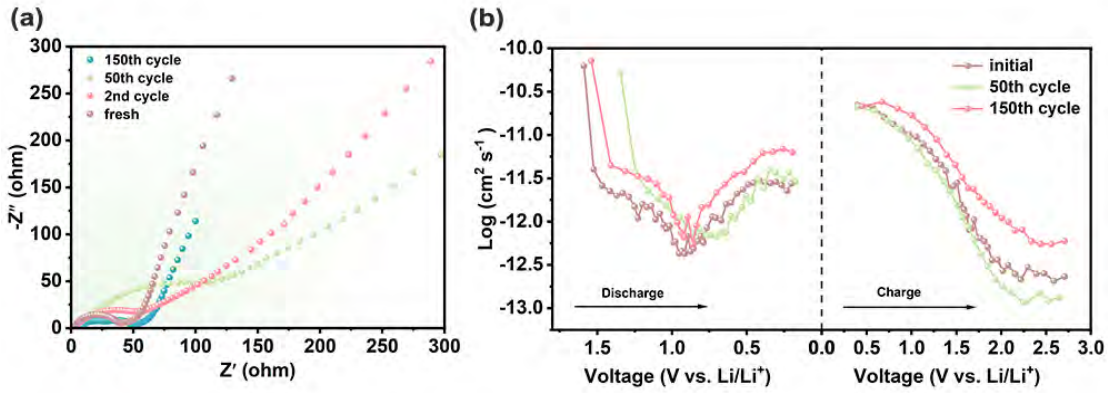

Fig. S11. (a) EIS spectra of different cycles; (b) GITT curves of different cycles.

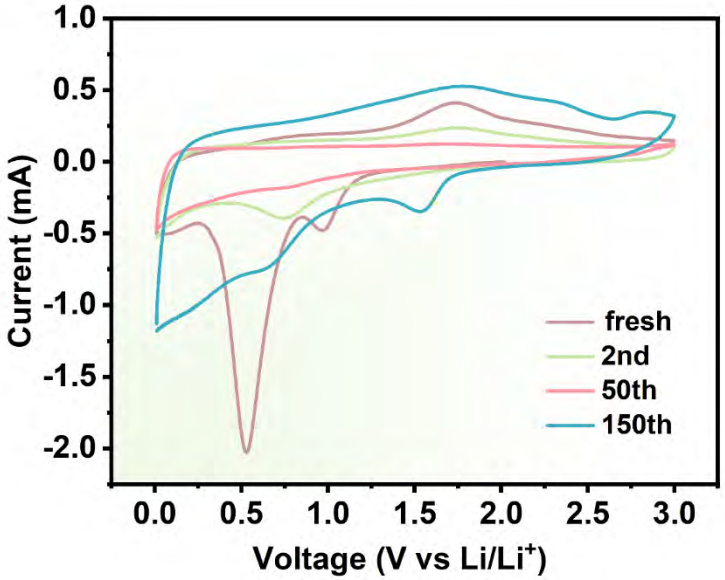

Fig. S12. CV curves of different cycles at 0.5 mV s^{-1}.